Coastal Jet Adjustment near Point Conception, California, with Opposing Wind in the Bight

DAVID A. RAHN

Atmospheric Science Program, Department of Geography, University of Kansas, Lawrence, Kansas

THOMAS R. PARISH AND DAVID LEON

Department of Atmospheric Science, University of Wyoming, Laramie, Wyoming

(Manuscript received 29 May 2013, in final form 29 October 2013)

ABSTRACT

Typical spring and summer conditions offshore of California consist of strong northerly low-level wind contained within the cool, well-mixed marine boundary layer (MBL) that is separated from the warm and dry free troposphere by a sharp temperature inversion. This system is often represented by two layers constrained by a lateral boundary. Aircraft measurements near Point Conception, California, on 3 June 2012 during the Precision Atmospheric MBL Experiment (PreAMBLE) captured small-scale features associated with northerly flow approaching the point with the added complexity of encountering opposing wind in the Santa Barbara Channel. An extremely sharp cloud edge extends south-southwest of Point Conception and the flight strategy consisted of a spoke pattern to map the features across the cloud edge. Lidar and in situ measurements reveal a nearly vertical jump in the MBL from 500 to 100 m close to the coast and a sharp edge at least 70 km away from the coast. In this case, it is hypothesized that it is not solely hydraulic features responsible for the jump, but the opposing flow in the Santa Barbara Channel is a major factor modifying the flow. Just southeast of Point Conception are three distinct layers: a shallow, cold layer near the surface with northwesterly winds associated with an abrupt decrease in MBL height from the north that thins eastward into the Santa Barbara Channel; a cool middle layer with easterly wind whose top slopes upward to the east; and the warm and dry free troposphere above.

1. Introduction

Strong wind near the surface along the Californian coast is common in the spring and is ultimately set up by the contrast in pressure between the thermal low over the southwest United States and the anticyclone over the cool Pacific Ocean. Associated with the subtropical branch of the Hadley circulation is downward motion that maintains a strong subsidence inversion that caps the marine boundary layer (MBL). During the spring and summer a general wind speed maximum extends along the California coast from Cape Mendocino to past Point Conception with a local maximum in the lee of Point Conception. Transient synoptic systems may also contribute to particularly strong wind events along the

Southern California shoreline. Localized maxima of wind speed are embedded within the broader low-level jet and occur along the coastline near changes in the orientation of the topography such as points and capes. The alongshore variability of the wind and other important parameters is described in depth by Dorman et al. (2000), Koračin and Dorman (2001), and Koračin et al. (2004).

The Froude number (Fr) is an important diagnostic variable for coastal flow. It is the ratio of the flow speed to the fastest possible gravity wave in the layer, which is proportional to MBL height and strength of the inversion. Typically, if the wind is strong within a shallow MBL, local variation along the coast is often attributed to mechanical forcing (e.g., Edwards et al. 2001; Haack et al. 2001). Strictly speaking in the ideal case, Fr of unity is transcritical. The calculation and meaning of Fr is imprecise in the real atmosphere because of departures from shallow-water theory. The ideal case is a homogeneous, single-layer fluid, while the real atmosphere is

Corresponding author address: David A. Rahn, Atmospheric Science Program, Department of Geography, University of Kansas, 1475 Jayhawk Blvd., 201 Lindley Hall, Lawrence, KS 66045-7613.
E-mail: darahn@ku.edu

variably stratified. However, it is the relative numbers that are important (Burk and Thompson 2004). For example, Rogerson (1999) showed that an expansion fan occurs if the approaching marine layer flow has Fr between 0.5 and 1. Mechanical features manifest as a compression bulge upwind of a cape as the flow slows and the MBL deepens, while an expansion fan occurs downwind of a cape as the flow speeds up and the MBL thins. These features are tied to the topography and are on the order of 10 km (Koračin and Dorman 2001). Features that resemble compression bulges and expansion fans have been observed by aircraft from Cape Blanco to Point Sur (Winant et al. 1988; Rogers et al. 1998; Dorman et al. 1999) and Point Conception using surface stations (Dorman and Winant 2000) and a numerical model (Skyllingstad et al. 2001). In addition, many modeling studies investigate mechanical features (e.g., Samelson 1992; Burk and Thompson 1996; Rogers et al. 1998; Burk et al. 1999; Rogerson 1999; Tjernström and Grisogono 2000).

Dorman and Koračin (2008) provide a particularly detailed analysis of the conditions near Point Conception, California, using surface observations, soundings, radar profilers, and high-resolution numerical simulations. They conclude that the synoptic setting is what fundamentally drives the northerly flow, and that marine layer hydraulic dynamics force the responses of a slowing and deepening of the layer upwind and a quickening and thinning of the layer downwind of the point. Alternate explanations that may force these features such as a diurnal thermal low or leeside flow down the Santa Ynez Mountains were deemed unacceptable.

Important details of this system are often missed because of the small-scale nature and difficultly in observing these features at a sufficiently high spatial resolution offshore near the top of the MBL. To address this issue, a field project called the Precision Atmospheric MBL Experiment (PreAMBLE) was designed to study such details of the lower atmosphere in the vicinity of the extreme bend near Point Conception. Few aircraft observations have been obtained offshore of Point Conception, but previous campaigns include Edinger and Wurtele (1972) and Rogers et al. (1998). Another case of a coastal jet on 19 May 2012 during PreAMBLE has been examined by Rahn et al. (2013), which had a transition of the northerly coastal flow around Point Conception under relatively stagnant conditions in the Santa Barbara Channel. The classic features described by the literature were present in the 19 May 2012 case, but other features such as the dilution of the temperature inversion as the MBL thins and off-continent flow above the MBL were highlighted with in situ and lidar data. In addition to the coastal jet, a prominent cyclonic circulation (the Catalina eddy) may develop in the California Bight, which is most frequent from late spring through early fall and has a regular diurnal cycle (Mass and Albright 1989).

The Catalina eddy and northerly flow around Point Conception are commonly treated separately. This work examines a case when there are strong winds transitioning around the point at the same time there is an opposing wind associated with a cyclonic circulation in the California Bight. Measurement systems and techniques are introduced in section 2. Results from the observations are shown in section 3 and are synthesized into a conceptual model at the end of that section. The main conclusions are briefly summarized in section 4.

2. Data

PreAMBLE used the University of Wyoming King Air (UWKA) as the primary observational platform and was based out of the Naval Air Station at Point Mugu, California, from 15 May to 17 June 2012. The vertical structure offshore is observed in situ by the UWKA as the aircraft ascends and descends. By flying on an isobaric surface and measuring the height, the UWKA can precisely map the horizontal pressure gradient force (PGF). Since the slope of the isobaric surface is related to the PGF, this is a critical component in diagnosing the forcing of atmospheric motion. Early work employed radar altimeters to obtain the height measurements (e.g., Rodi and Parish 1988), but more recently differential GPS processing is used because it provides a more accurate measurement (Parish et al. 2007). The gentle slope of an isobaric surface requires that the height needs to be known to within a fraction of a meter. For example, a $10 \, \text{m s}^{-1}$ geostrophic wind at 43°N is associated with an isobaric height change of 10 cm every kilometer. Precise measurements are critical. The aircraft autopilot deviates off of the exact isobaric surface, but any deviation is corrected with the hypsometric equation that also requires an accurate static pressure measurement. This technique has been proven in previous cases (e.g., Rahn and Parish 2007) and details can be found in Parish et al. (2007) and Parish and Leon (2013). An additional concern in applying this method is that any pressure change over time during the flight must be known since it would alter the slope. Simply flying reciprocal legs alleviates this problem since repeating the same leg in the opposite direction reveals any time tendency that can be corrected given the measured rate of change of height with time.

Part of the instrument payload on the UWKA during PreAMBLE was the Wyoming Cloud lidar (WCL), which was configured with upward- and downward-looking beams. The WCL is a 355-nm lidar designed for retrieval of cloud and aerosol properties. The returned
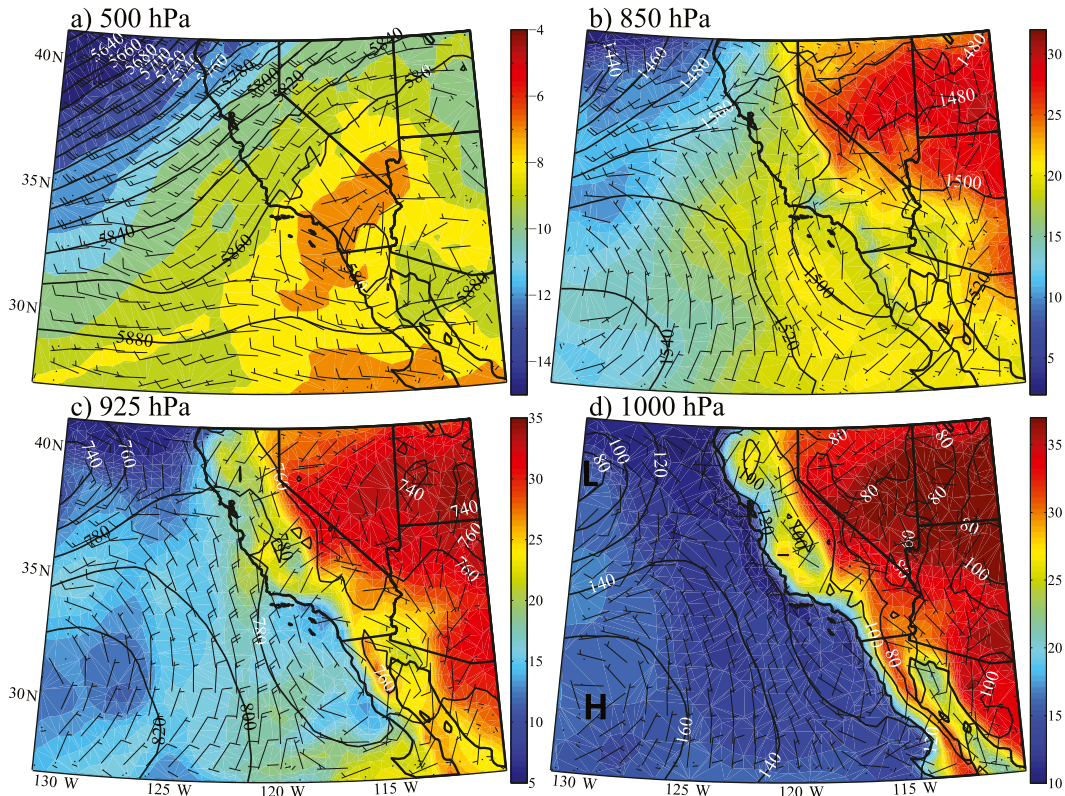
FIG. 1. Isobaric maps at 1800 UTC 3 Jun 2012 depicting height (m, contours), temperature (°C, color), and wind barbs (m s^{-1}; short ticks = 5 m s^{-1}, long ticks = 10 m s^{-1}) at (a) 500, (b) 850, (c) 925, and (d) 1000 hPa. Data are from the 0.5° grid of the Climate Forecast System Reanalysis (Saha et al. 2010).

signal for the upward-looking lidar is sampled at 3.75-m intervals, while the signal for the downward-looking lidar is sampled at 1.5-m intervals. Additional details of the WCL can be found in Wang et al. (2009) and Wang et al. (2012). The lidar data are combined with inertial navigation system/GPS data from the UWKA to produce time–height images of the (uncalibrated) attenuated backscatter. The WCL is well suited to determine cloud boundaries, but because the lidar signal is rapidly attenuated in cloud, the lidars are unable to penetrate deeply into the cloud layer. Lidar data have been collected in the past during Coastal Waves 1996 (Rogers et al. 1998); however, an important advancement is the depolarization ratio, which assisted in the interpretation of the transition region.

3. Results

a. Overview

On the morning of 3 June 2012 an upper-level trough extended over much of the Pacific and a ridge was situated over the mountain west (Fig. 1). A surface cyclone centered west of Northern California near 38°N, 131°W

disrupted and displaced the climatological Pacific anticyclone toward the south of its June climatological position at 34.0°N, 143.7°W (Schroeder et al. 2013). A zonal pressure gradient along the central California coast continues offshore of Southern California driving north-northwest winds over this area. A cyclonic circulation in the California Bight is present in the synoptic maps indicative of a Catalina eddy (e.g., Wakimoto 1987; Mass and Albright 1989; Thompson et al. 1997; Parish et al. 2013).

A variety of buoy and surface stations are located in Southern California (Fig. 2). Unfortunately, during Pre-AMBLE buoy 46025 was not operating and buoy 46011 did not have any wind reports. Observations of the wind demonstrate the strong northerly alongshore wind from buoy 46042 to buoy 46054 (Fig. 3). The coastal station of pslc1 exhibits light and variable wind since it is sheltered from the northerly flow and draws attention to the fact that coastal stations are not always representative of the flow just offshore. From buoy 46053 and southward, the wind is generally from the south, and over the 4 days there is a diurnal signal. During the day there is a stronger onshore flow associated with the afternoon sea breeze. At
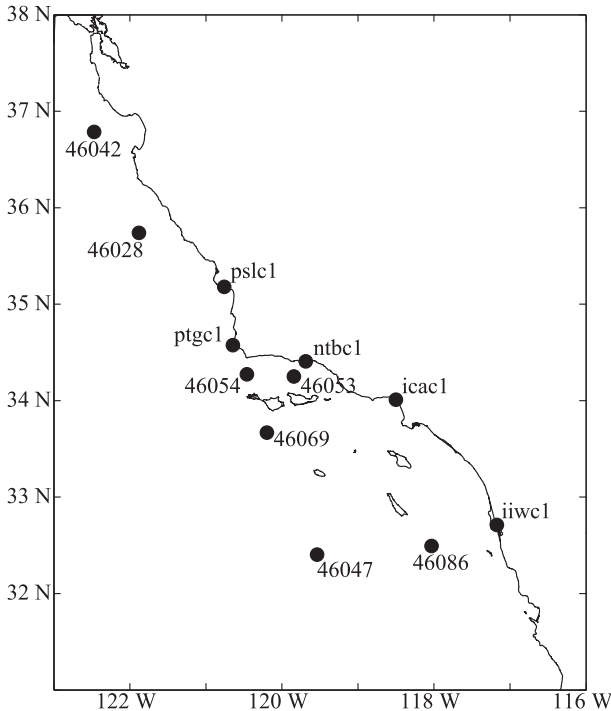
FIG. 2. Locations of buoy and coastal surface stations.

FIG. 3. Surface wind vectors (m s^{-1}, scale at top right) at buoy and surface stations along the California coast that are indicated at the top left of each time series.

the offshore buoys 46069 and 46047 the wind was consistently from the northwest, and at 46086 the wind was westerly from 0000 UTC 1 June to 1200 UTC 2 June and light and variable afterward (not shown).

Observations of mean sea level pressure along the coast are shown in Fig. 4. To eliminate the influence of pressure tides on the 10-h evolution, the average diurnal cycle of surface pressure is removed. The surface pressure along the coast reveals that from 1200 to 2200 UTC there is an alongshore pressure gradient pointed toward the south from buoy 46042 to pslc1. At 1200 UTC there is also an alongshore pressure gradient pointed to the south until icac1, but the pressure increases at iiwc1. Over the morning and into the afternoon, the pressure gradient from iiwc1 to ntbc1 reverses such that there is an alongshore pressure gradient pointed to the north. In the afternoon when the flight took place, there are opposing alongshore pressure gradients with a local pressure maximum at ptgc1 that is ~1 hPa greater than the nearby stations of pslc1 and ntbc1.

Preflight conditions suggested the development of a sharp cloud boundary throughout the morning as initially inferred from an animation of satellite imagery. Morning cyclonic circulation in the Southern California Bight was common during the field campaign, but varied in extent and intensity and often dissipated before the late afternoon when a majority of the flights took place. The flight strategy for this mission was to map the isobaric
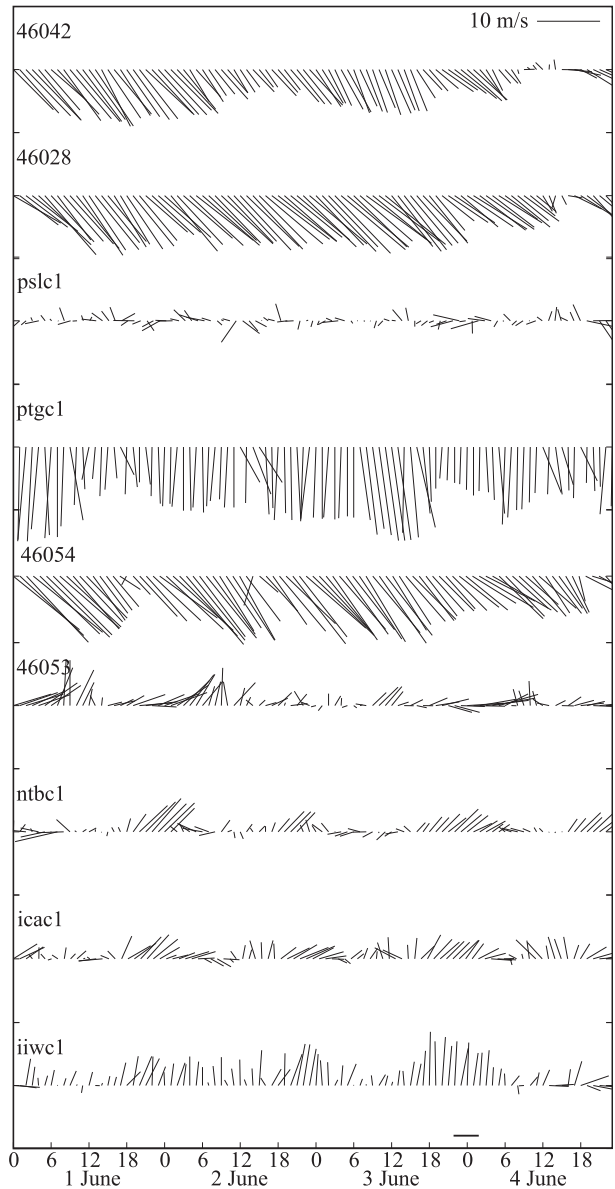
surface along the cloud edge by flying a spoke pattern emanating from a point halfway between Point Conception and San Miguel Island on the western edge of the Santa Barbara Channel (Fig. 5). This pattern was flown along an isobaric surface in one direction starting with the first leg in set A followed by additional isobaric legs farther south with a sounding at the end of the final pattern leg at E. After the sounding, the pattern was repeated in reverse. While airborne, air traffic control allowed the flight plan to be modified toward the end by terminating the return leg of set B early and allocating that flight time
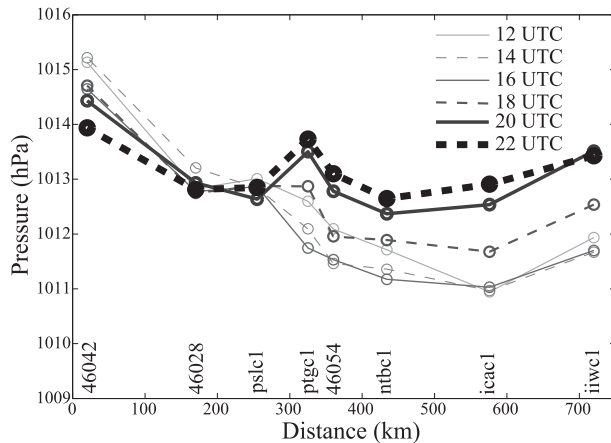
FIG. 4. Surface pressure (hPa) on 3 Jun 2012 every 2 h along the coast with the average diurnal cycle removed. Distance (km) is calculated by following the coastline and locations of the observations are indicated on the bottom.

to instead fly above the clouds and use the downward-pointing lidar to continuously detect the MBL top as it abruptly dropped in height along set A. During the ferry through the Santa Barbara Channel to and from the center of the spoke pattern, the aircraft performed a series of ascents and descents culminating in a sawtooth pattern to obtain the vertical structure. Measurements from the individual isobaric legs are discussed first and then after examining the aircraft soundings, a broader conceptual model is proposed that synthesizes the available data.

b. Isobaric legs

Measurement of the height change with distance along an isobaric surface enables the PGF to be determined directly from in situ observations. To correctly calculate the PGF, any changes of the height of the isobaric surface over time (referred to as the height tendency) must be taken into account since it can skew the data toward stronger or weaker PGF than reality (Rodi and Parish 1988). Height tendency is typically attributed to synoptic-scale features and can be applied to the entire flight. To alleviate this problem, the spoke pattern was not only repeated flying in the opposite direction to get an isobaric tendency, but the aircraft passed over the same point at the center of the spoke pattern at the end of every leg. Isobaric heights fell at an average rate of $0.0007 \, \mathrm{m \, s^{-1}}$. This cannot be neglected because it corresponds to a height fall of 7.5 m over a 3-h period. Flight time for this mission was 3.7 h. The following analysis takes the height tendency into account by correcting the isobaric height by $0.0007 \, \mathrm{m \, s^{-1}}$ times the number of seconds from the beginning of the first leg of the set.

Beginning with the reciprocal set of legs closest to the coast (set A), it is not surprising that a large gradient in the isobaric surface (Fig. 6) exists close to the terrain based on the standard conceptual model of an expansion fan (e.g., Winant et al. 1988; Dorman and Koračin 2008) and other flights during PreAMBLE (Rahn et al. 2013). In the north the isobaric surface rises, which implies a deeper MBL. Concurrently, the wind speed decreases,
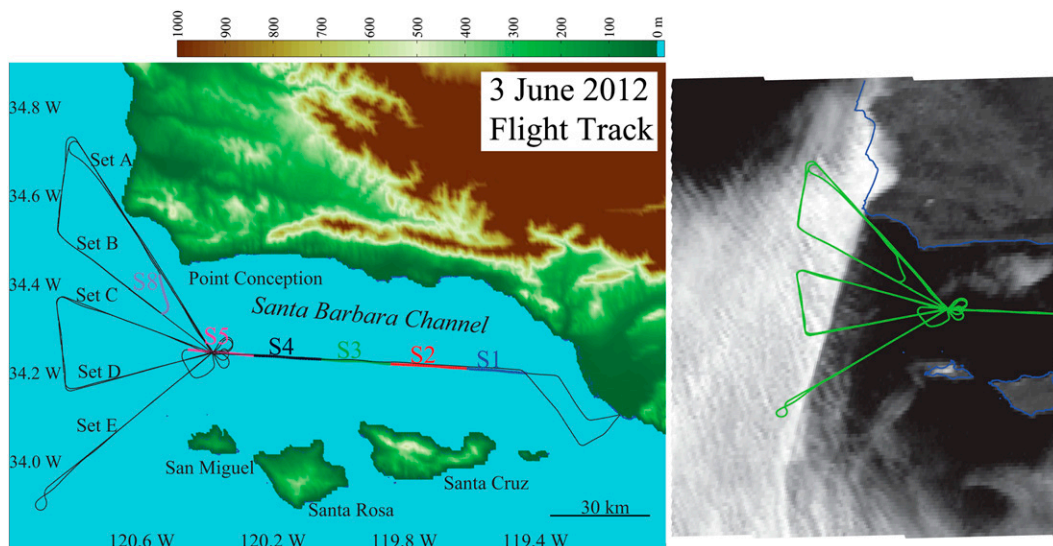

FIG. 5. (left) Topographic elevation (m) and flight track on 3 Jun 2012. Location of soundings along the flight track are indicated by colors and labeled with S and the sounding number. (right) Visible satellite image at 2100 UTC 3 Jun 2012 with the flight tracks overlaid.
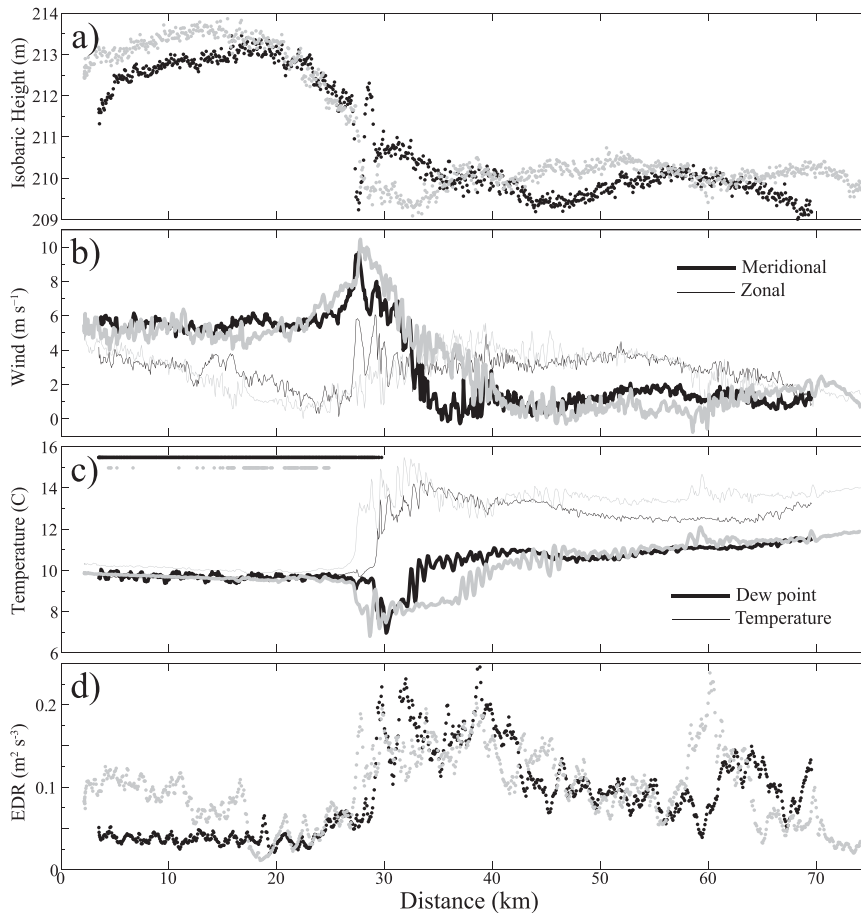
FIG. 6. In situ aircraft data for set A with westernmost end of leg to the left. Black is used for the first leg and gray for the returning leg. (a) Corrected isobaric height (m), (b) negative meridional wind component (m s^{-1}, bold) and zonal wind component (m s^{-1}, thin), (c) temperature (°C, thin), dewpoint temperature (°C, bold), and presence of liquid water indicated by the dots near 15°C, and (d) eddy dissipation rate (EDR, m^2 s^{-3}).

but mainly the zonal wind component decreases, which reflects the north-northwest wind impinging on the terrain and being forced around the terrain and becoming more northerly. This is consistent with a compression bulge. A sharp wavelike feature is detected in the first leg (black) but not the last leg (gray). The wind speed increases from the compression bulge through the abrupt drop of the MBL top.

Since the aircraft is flying at a constant level and the top of the MBL lowers rapidly toward the southeast, the aircraft is above the cool and moist MBL in the southeast. Above the MBL the isobaric surface along the flight track is relatively flat and winds weaken to about 2 m s^{-1}. The temperature and dewpoint clearly mark the location where the aircraft flies through a temperature inversion. The temperature indicates that the aircraft is within the MBL until just before 30 km where it increases by about 4°C while the dewpoint drops. The presence of

liquid water is indicated in Fig. 6c and corresponds to the same location that the aircraft passes through the inversion. Dissipation of the cloud over the flight is revealed by the difference between the first (black) and last (gray) leg. While the temperature clearly increases out of the MBL, the dewpoint initially decreases 1°–2°C but then increases again to values actually greater than that found in the MBL toward the northwest.

A conspicuous feature of all the measurements near the sharp decline over a short horizontal distance in MBL height is the apparent noise in the signal suggested by the rapid fluctuations in the wind, temperature, and moisture. Noise in the isobaric height measurements is more subtle, but compared to the measurements farther away from the coastline, there is slightly more spread in the data. The noise is not an artifact of the measurements but is attributed to the real atmospheric conditions, primarily enhanced turbulence in the vicinity of
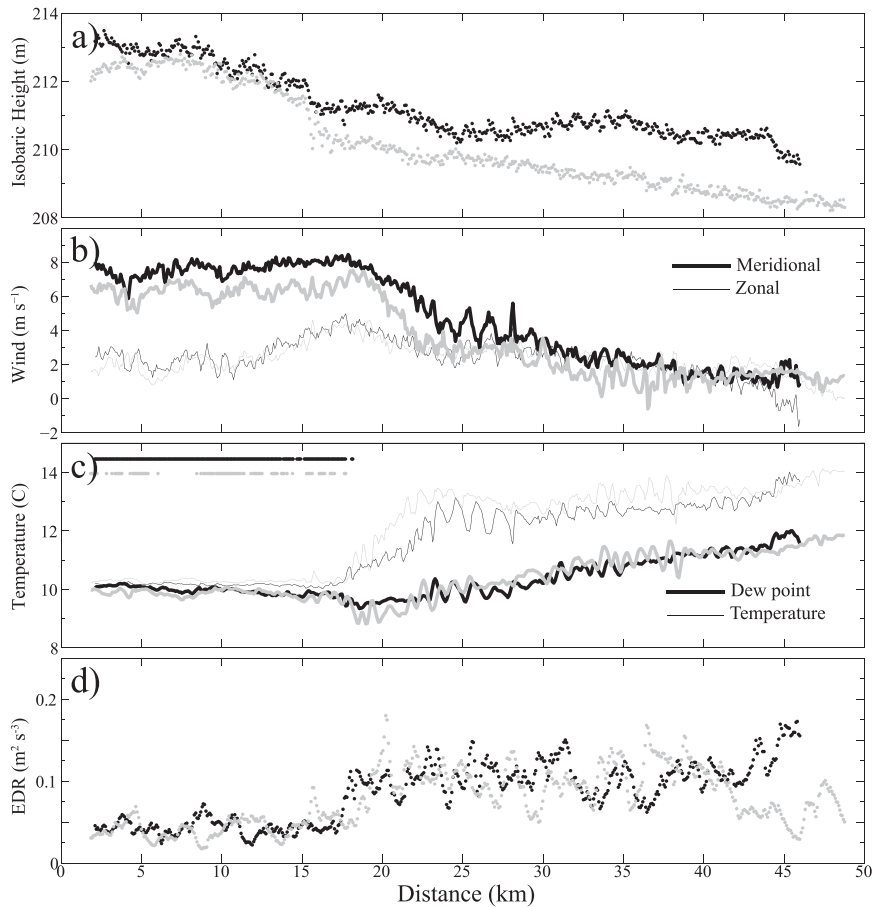
FIG. 7. As in Fig. 6, but for set C.

the sharp MBL height drop and large wind shear. The eddy dissipation rate (EDR) is a measure of turbulence using the method developed by MacCready (1964) with higher values corresponding to more turbulence. There is a spike in turbulence as the aircraft crosses the temperature inversion and encounters large changes in wind speed and direction. Thus, the greater EDR values are likely enhanced by the mechanical generation of turbulence by wind shear. Toward the southeast, the turbulence decreases but there are noticeable spikes such as at 60 km in the second (gray) leg. Soundings shown later also indicate a large vertical wind shear near this flight level that contributes to the mechanical production of turbulence.

In each of the isobaric legs of the spoke pattern there is a continuous transition from north to south. For brevity, only sets A, C, and E are shown. Observations from set C (Fig. 7) depict many of the same features although the transition from west to east is less pronounced. A small jump in the isobaric height is present at ~15 km in both legs with the second leg exhibiting a slightly more prominent jump. An increase of temperature near 18 km

is associated with the cloud edge. Enhanced turbulence is again evident in the fluctuations of all the variables, but measurements of EDR indicate a slightly lower value than set A. Once again, the dewpoint temperature increases toward the east after the aircraft passes through the temperature inversion. Another difference with the previous legs is that toward the extreme east end of the leg the wind is from the east.

Set E comprises the southernmost isobaric legs directed along a northeast–southwest axis and the UWKA reaches the sharp cloud edge at the western end of the leg (Fig. 8). The isobaric height is linear with little indication of any sort of jump. Both wind components decrease linearly toward the northeast. Winds are $\sim 10\,\mathrm{m\,s^{-1}}$ from the north-northwest along the western portion of the leg. At the eastern end of the leg, wind directions have switched to easterly at $\sim 2\,\mathrm{m\,s^{-1}}$. Geostrophic wind perpendicular to the flight track (roughly northwest) is $13\,\mathrm{m\,s^{-1}}$, so the wind is subgeostrophic and should accelerate toward the east, but the acceleration of the flow is against an easterly wind. After passing through a weak increase of temperature, the dewpoint increases
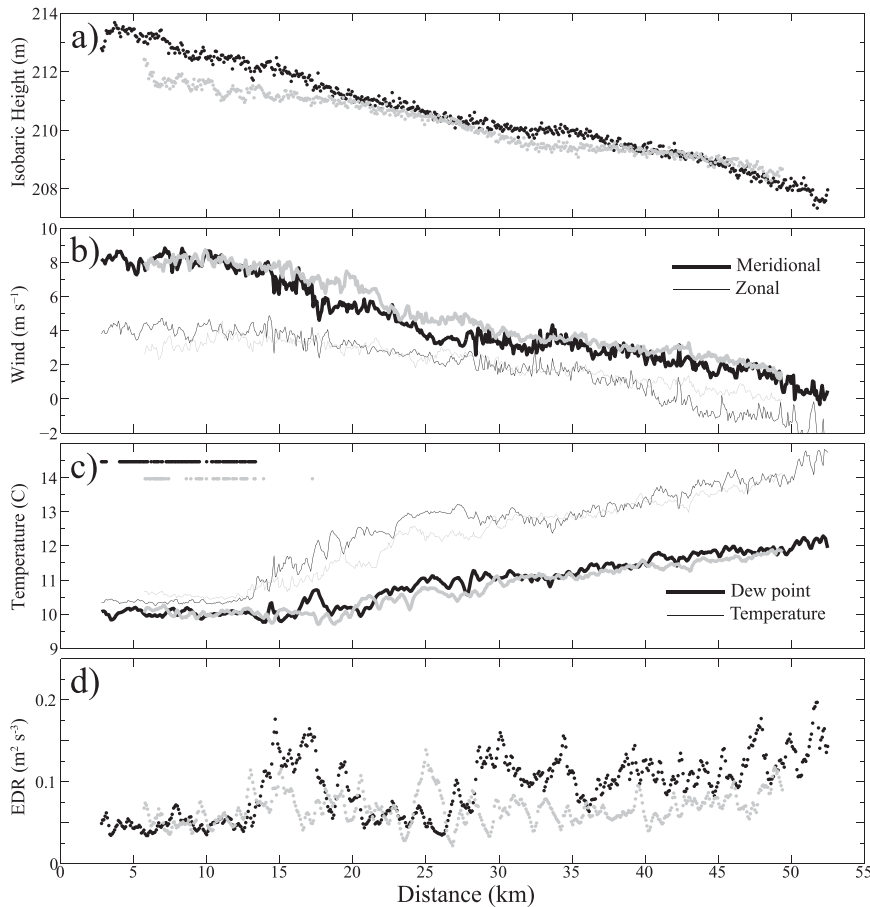
FIG. 8. As in Fig. 6, but for set E.

to values above that found in the MBL to the southwest. Turbulence is slightly elevated, but a region of reduced turbulence is found near a distance of 20 km that is also reflected in the temperature and wind measurements that show less variance.

c. Synthesis of isobaric measurements

There are several important features that the isobaric legs illustrate. In set A the locally deeper MBL and slower flow that is deflected around the cape is consistent with a compression bulge northwest of the point. Set A also contains the most pronounced changes including a 4-m drop in the isobaric height over a horizontal distance of just ~15 km. For perspective, the geostrophic wind associated with that height gradient is 33 m s^{-1}. According to the Bernoulli equation, when the MBL decreases in height, the wind speed increases. This is exactly the case here where the wind increases from 6 m s^{-1} in the northwest to 8 m s^{-1} as the MBL depth decreases. Part of the motivation for flying the spoke pattern was to directly measure the isobaric

heights, which enables a spatial depiction of the height field. Figure 9 illustrates the isobaric heights from the first entire spoke pattern that are corrected for time tendencies and interpolated between the legs. Isobaric height clearly drops from the northwest into the Santa Barbara Channel. A relatively flat isobaric surface exists near the center of the spoke pattern since the aircraft exited the northern MBL, which has much greater horizontal variability in the western region.

Measurements of the isobaric height indicate a concentrated zonal gradient of isobaric height that is consistent with the sharp cloud edge. As seen in the individual sets of legs (Figs. 6–8), the largest isobaric height gradient is encountered during set A. To the south the height gradient is weaker, but is still associated with the cloud edge. In sets C and E, the features are similar to set A, although not as well defined. Isobaric height contours indicate a compression bulge just northwest of the point since there are locally high heights, which also appear to be detached from the high heights farther toward the south. The localized nature of the high
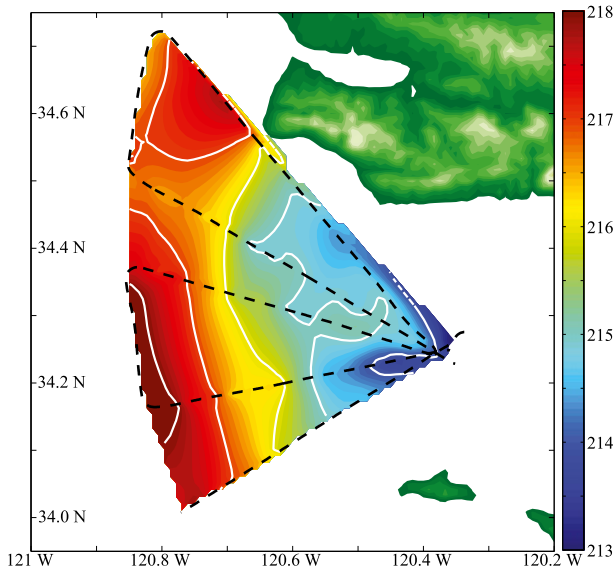
FIG. 9. Isobaric height (m) contours for the first spoke pattern flown. Flight tracks overlaid as black dashed contours and topography is shown using the same color scale as in Fig. 5.

heights north of the cape is consistent with the idea that mechanical features such as a compression bulge do not extend far from the topography and are on the order of 10 km or so (Koračin and Dorman 2001). While mechanical features play the greatest role near the coast, observations suggest that other features may be responsible for the sharp cloud edge that extends much farther to the south. Furthermore, the large jump in the isobaric height as detected in set A is unlikely to be so sharp from mechanical effects alone, and other factors may be contributing, such as an interaction with the opposing wind in the Santa Barbara Channel.

d. Vertical structure

A lidar can readily identify features of the lower atmosphere, especially the top of the MBL and any cloud-free layers. Because clouds northwest of Point Conception quickly attenuated the lidar signal during the low-level isobaric legs, an additional flight leg along the same flight track as set A but above the MBL at about 700 m was flown to obtain a continuous measurement of the MBL height from the downward beam of the WCL (Fig. 10). From the farthest point to the northwest the MBL depth increased to a maximum near 2325:00 UTC before slightly decreasing in height. At 2323:30 UTC the cloud ended abruptly, consistent with the satellite imagery. The abrupt drop of the MBL height is much sharper than the transition that occurred on 19 May 2012 under relatively quiescent conditions in the California Bight (Rahn et al. 2013). On 19 May the MBL height dropped 200 m over 20 km. The reflectivity for the

3 June case indicates a sudden drop from 400 to 100 m over just tens of meters. Figure 10 also indicates that a low layer of high reflectivity remains below ~100 m and extends well to the southeast. There is a weaker boundary in the cloud-free region to the southeast that slopes down from 500 m at the far southeastern end of the domain to 300 m just before the sharp change of MBL depth. Between the nearly vertical drop of the cloud-capped MBL to the northwest and the cloud-free boundary to the southeast there is apparently a gap between the two layers. The EDR indicates enhanced turbulence at this location.

Additional lidar data from set B are used to highlight the vertical structure. A lidar image from set B is shown in Fig. 11 and is similar to the previous lidar image with a few exceptions. The sharp change of MBL height is not continuously detected because the flight level is at approximately 200 m and the beam is quickly attenuated by droplets when flying in the cloud. Nevertheless, this illustrates the layers in the southeastern portion more clearly. The downward-pointing lidar detects a shallow layer with a top near 100 m, consistent with that seen in the previous image. The upward-pointing lidar detects a deep layer in the Santa Barbara Channel that increases from ~400 m at the 2124 UTC/45 km mark and increases to ~600 m at the eastern edge. A thin cloud exists at the top of the upper layer in the far southeast, which is present in the satellite image as well.

Three distinct layers are detected by the lidar in the southeast. Properties of these three layers are obtained by in situ measurements from the UWKA. On the ferry out and back from the center of the spoke pattern, the UWKA conducted a series of vertical ascents and descents. The final descent from the outbound ferry is depicted by the green line in the satellite image and is just east of the lidar image. The temperature profile above 500 m reveals the classic subsidence inversion where the temperature increases and dewpoint decreases. The capping temperature inversion is not concentrated in a narrow region but is fairly deep (500–800 m). Below the subsidence inversion at 500 m the temperature profile follows a dry adiabatic lapse rate indicating a well-mixed layer. Just below the subsidence inversion the dewpoint indicates saturation, consistent with the lidar and satellite observations of a thin cloud. Below 300 m the temperature no longer follows the dry adiabatic lapse rate and becomes a few degrees cooler than the air above, representing another cooler, stable layer below.

Perhaps the most compelling evidence of the existence of three distinct layers is the wind profile. Wind direction is from the northwest in both the upper layer and lower layer. In the upper layer the wind speed approaches $10\,\mathrm{m\,s^{-1}}$. In situ measurements in the lowest
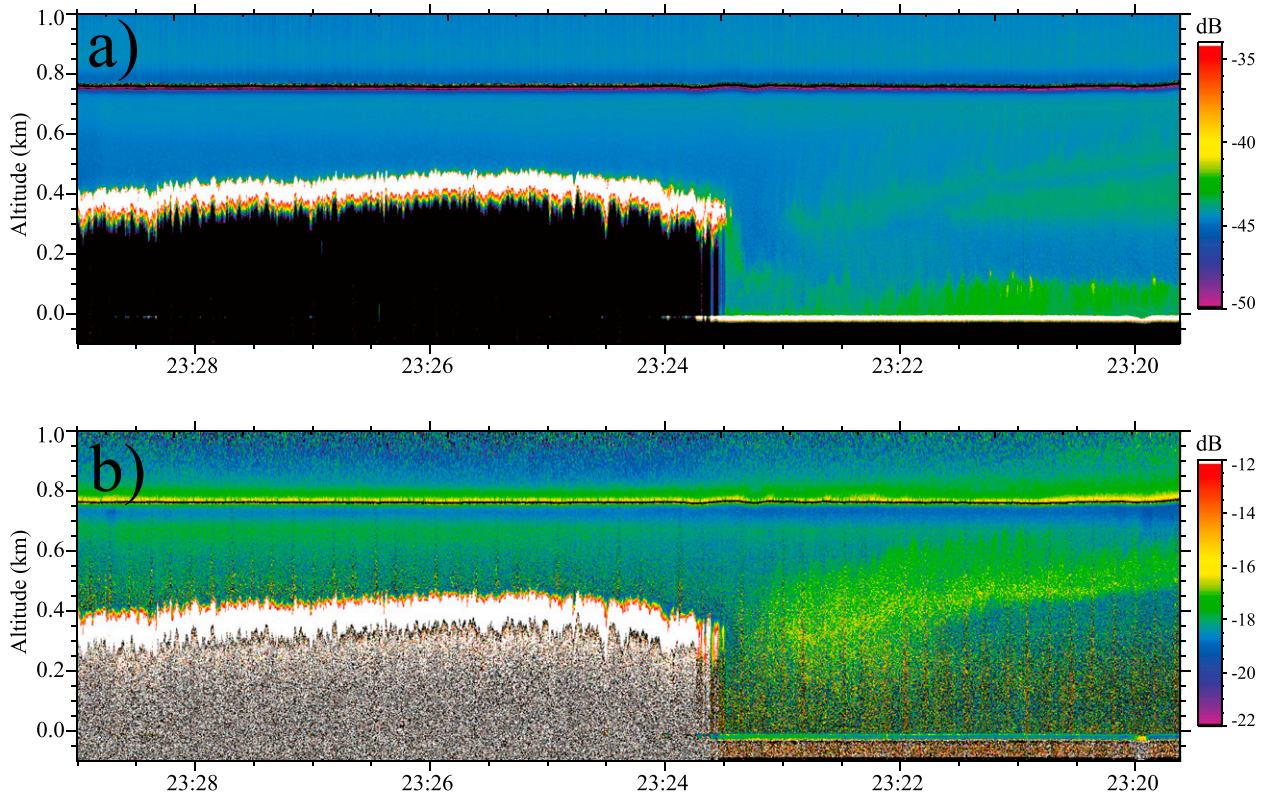
FIG. 10. Lidar returns of (a) reflectivity (dB) and (b) depolarization (dB) over set A. West is to the left. Aircraft elevation is about 750 m as indicated by the black line near this height.

layer ($\sim$150 m) indicate a wind speed of $\sim$6 m s^{-1}, but the maximum wind is likely slightly above 6 m s^{-1} since the trend is increasing with lower height, which must again decrease near the surface because of friction. The change of wind direction is abrupt, though the wind speed follows a slightly smoother transition. The most striking feature of the wind profile is seen in the middle layer where the wind is easterly, opposing the north-westerly wind originating from the north of Point Conception. The middle layer is well mixed since the vertical profile of temperature follows a dry adiabatic lapse rate. Wind measurements also reflect a well-mixed middle layer since both wind speed and direction are uniform. This layer is thought to be part of the re-sidual circulation associated with the Catalina eddy. This sounding is taken around buoy 46054 (Fig. 2), which had persistent northwest wind. This really high-lights the importance of obtaining a vertical profile that can capture a flow moving in the opposite direction just above the surface.

Sounding 8 was taken closer to the abrupt drop in the MBL height near Point Conception (Fig. 5). The wind and temperature profiles also reveal three distinct layers (Fig. 12). The temperature profile is not as well defined

as that in Fig. 11, which may be attributed to the greater vertical mixing associated with the larger turbulence indicated by the EDR in the isobaric legs. The wind speed and direction clearly demark the transition between the westerly flow below, southeasterly flow in the middle, and northwesterly flow above. The middle layer is only 100 m thick as opposed to the 250-m-thick middle layer seen in Fig. 12, which is consistent with the lidar image that de-tects a thicker middle layer in the east that thins toward the west. It is also interesting to note that the wind is actually from the southeast in the middle layer, while sounding 11 indicated easterly wind in the middle layer.

To extend the analysis of the layers in the Santa Barbara Channel, the sawtooth pattern flown by the aircraft using soundings 1 through 5 is used to construct a cross section of potential temperature and wind (Fig. 13). The flight track is represented by the thick dashed line and the height of the layers is marked by a black dot. The layer heights are subjectively determined from the individual soundings shown in Fig. 14 using information from the temperature, dewpoint, and wind. Some heights are not as well defined as others, but the divisions are thought to be fairly representative of the layers. For instance, in sounding 2 there is a discontinuity
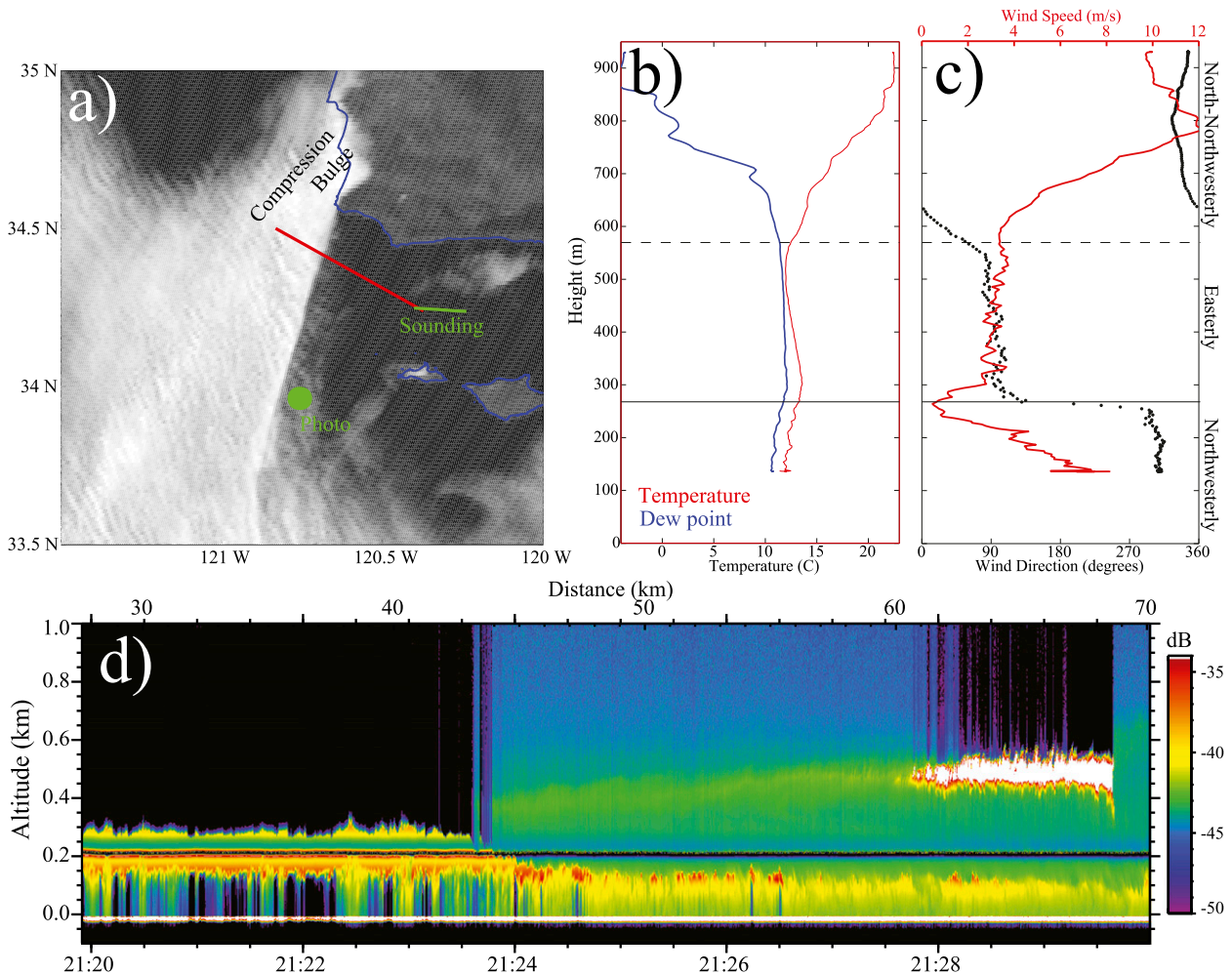
FIG. 11. (a) Visible satellite image with location of lidar image in red, sounding in green, and location of picture in Fig. 16 given by the green circle; (b) profile of temperature (°C, red) and dewpoint temperature (°C, blue); (c) profile of wind speed (m s^{-1}, red) and wind direction (degrees, black); and (d) lidar reflectivity (dB) with west to the left and the aircraft elevation was ~0.2 km as represented by the black line at that height.

in the adiabatic profile of the temperature around 250 m and a small jump in the wind speed as well.

The meridional wind in Fig. 13 is strongest in the west at upper levels where there is strong northwesterly flow. In the middle layer the meridional component is light from the south. In the lowest layer the meridional wind is light from the north. The isentropes slope up from west to east above 600 m, consistent with the slope of the topmost temperature inversion. Stability is near neutral below that temperature inversion and the subtle temperature changes are not as easily seen in the interpolated cross section then they are in the individual profiles. However, the zonal wind displays clear differences. In the lowest layer (below ~200 m) the zonal wind is westerly and either shifts to easterly in the middle layer or is light. There is a 4–6 m s^{-1} zonal wind above 600 m, which is easterly for soundings 1–3 and westerly for soundings 4 and 5.

e. Numerical modeling

While this study is primarily based off of observations, numerical models typically provide additional information to assist in the analysis. Numerical simulations ranging in their complexity are often used as the basis for describing the coastal flow (Samelson 1992; Burk and Thompson 1996; Rogers et al. 1998; Burk et al. 1999; Rogerson 1999; Tjernström and Grisogono 2000; Skyllingstad et al. 2001). Products from operational models were used during the field campaign to support the forecasting and guide the flight plan for the following day. Characteristics of the circulation in the California bight predicted by operational models were often diverse. For the 3 June 2012 case, the Weather Research and Forecasting Model (WRF; Skamarock et al. 2008) was run after the field campaign in hopes of supplementing the observational data.
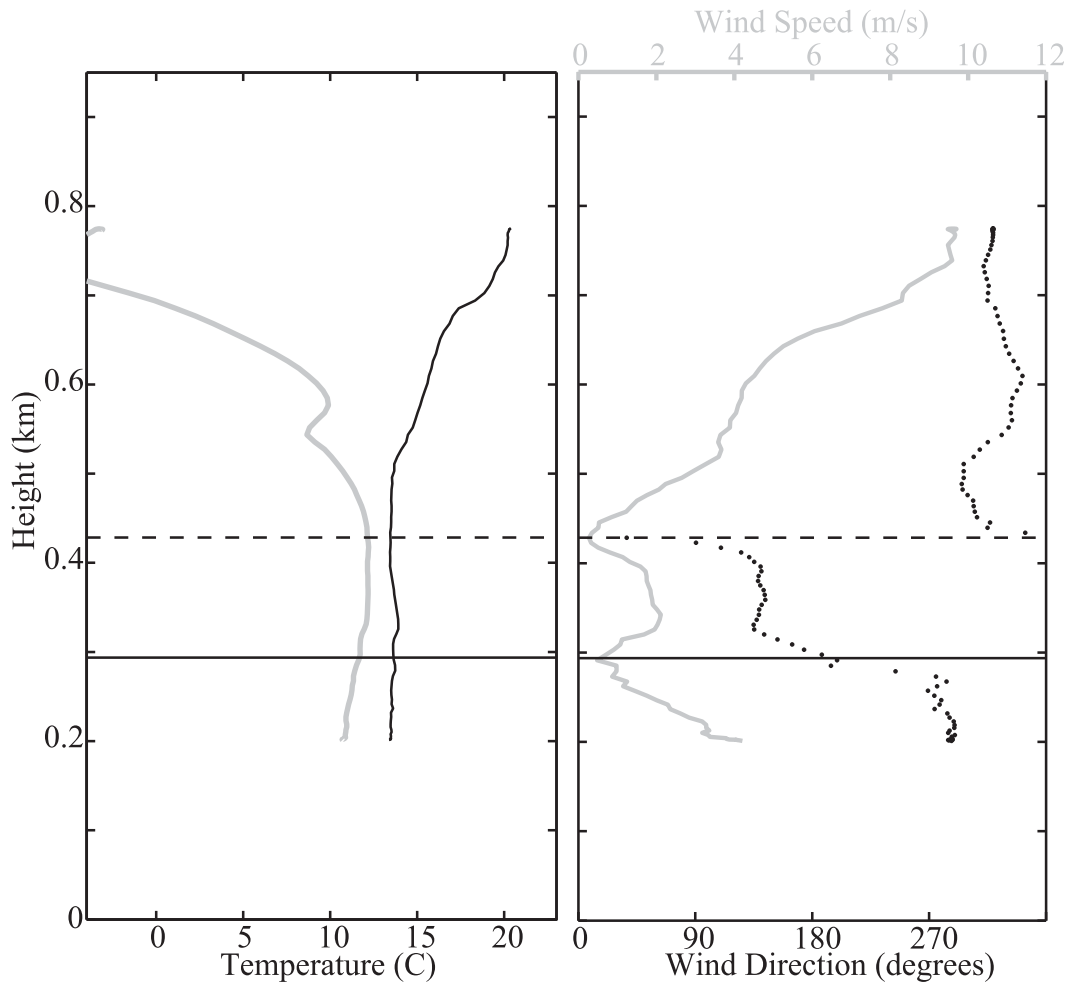
FIG. 12. Profiles of (left) temperature (°C, black) and dewpoint temperature (°C, gray) and (right) wind speed (m s^{-1}, gray) and wind direction (degrees, black dots). Subjectively determined layers indicated by the horizontal lines.

The WRF simulation is initialized at 0000 UTC 3 June by the 12-km North American Mesoscale Model (NAM) analysis grids that also provide the lateral boundary conditions of the mother domain during the simulation. The model domain consists of three nested grids centered over Point Conception. The innermost domain has 181 × 151 grid points with a horizontal grid spacing of 2 km. There are 70 vertical levels with telescoping spacing starting at 40 m near the surface and increasing to 100 m near 2 km. At this resolution, 14 different configurations were used. In addition, several 1-km runs were tested, different analysis grids were used to initialize the simulation, and different initialization times were used. None of those showed any clear improvement.

As an example, temperature and wind observations of soundings 3 and 5 are shown alongside model output for the 14 different configurations at a 2-km grid spacing (Fig. 15). Clearly, not only is the simulation sensitive to the choice of parameterization, but also all

configurations have difficulty representing the observed features. The temperature inversion occurred at a lower level than the observations and is associated with strong north-northeasterly wind above 600 m, which suggests an overabundance of warm, dry air being advected from the land to the north. Details of the three layers in sounding 5 are missed, so while the observations show clear layering, the model solutions do not.

Our intention here is only to illustrate why model data are not helpful in diagnosing this case, not to detail every single model configuration that was tried. Based on the complexity of the flow and the subtle forcing that occurs, it is certainly a challenging modeling problem. It may be worthwhile to state that based off of the combined least root-mean-square error between the observed and modeled temperature and wind, the best performance was for the following configuration: Pleim–Xiu scheme for planetary boundary layer (Pleim 2007), surface layer
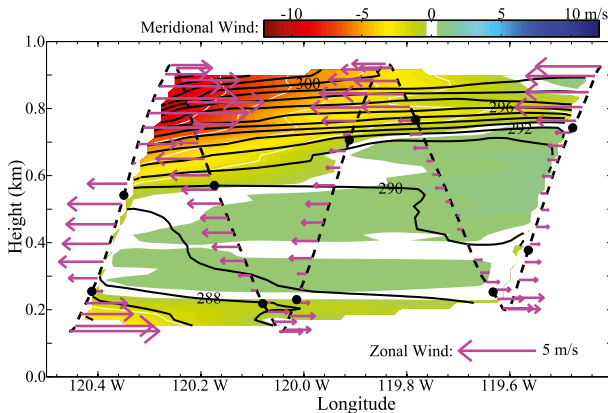
FIG. 13. Cross section of the sawtooth flight pattern conducted in the Santa Barbara Channel, which is constructed from soundings 1–5. Flight track indicated by the bold dashed line. The potential temperature (K, black lines) and meridional wind (m s^{-1}, color scale) are interpolated between soundings. The zonal wind vectors (m s^{-1}, magenta vectors with scale at bottom right) are plotted along the flight track every 12 s.

(Pleim 2006), and land surface (Xiu and Pleim 2001; Pleim and Xiu 2003), combined with the Goddard longwave radiation (Chou and Suarez 2000), the Dudhia shortwave radiation (Dudhia 1989), and Thompson microphysics (Thompson et al. 2008). Even the best configuration out of 14 had difficulties, indicating that although the models may give apparently reasonable results, without comparing the model output to measurements the actual atmosphere may be quite different than simulations depict.

f. Conceptual model

From the above measurements the following conceptual model is proposed. North of Point Conception, a classic MBL structure exists consisting of a single well-mixed layer capped by a strong temperature inversion at cloud top, and will be referred to as the "northern MBL." In the northern MBL the flow impinges on the terrain near Point Conception, slows, and deepens, which forms a compression bulge (Figs. 6 and 10). As the flow continues south and transitions around the point, an expansion fan can develop. Although the characteristic thinning of the northern MBL is present, classic expansion fan development is likely modified by other factors. A purely mechanical flow transition near the point is convoluted since in the Santa Barbara Channel there is an MBL (referred to as the "southern MBL") of comparable height to the northern MBL. The southern MBL is capped by a clear temperature inversion and the flow in the California Bight (away from Point Conception) exhibits a cyclonic circulation evident in the buoy data, animations of the satellite imagery, and even the coarse reanalysis.

As the northwesterly flow in the northern MBL rounds Point Conception, the MBL depth decreases abruptly (Fig. 10) and the wind near a height of 200 m increases from 7 to 10 m s^{-1} (Fig. 6), which is the general expansion fan response. However, the flow also encounters the southern MBL that is associated with the circulation of the Catalina eddy, which has been moving westward in the Santa Barbara Channel throughout the morning. At a flight level just above 200 m, the aircraft flies from the northern MBL into the southern MBL and the temperature increases from 10° to 13°C along the isobaric flight level. The difference between the northern and southern MBL temperature is reflected in sea surface temperature. At 2200 UTC 3 June 2012, measurements at buoy 46053 near Santa Barbara indicate an air temperature of 14.4°C and a water temperature of 15.1°C. Buoy measurements just north of Point Conception at 46011 near Santa Maria indicate an air temperature of 11.0°C and water temperature of 10.6°C. The difference in temperature is likely due to greater coastal upwelling north of Point Conception that is associated with the strong equatorward winds. The air coming from the northwest is colder than that to the south and the cooler, lower-level flow is from the northwest and the flow in the slightly warmer layer above is from the east. Given that information, the northwesterly flow is slightly cooler and denser so it must move underneath the layer with easterly flow that is slightly warmer and less dense.

Not only does sounding 5 (Fig. 11) show the layer of easterly wind but also in sounding 8 (Fig. 12), which is closer to the sharp cloud edge near Point Conception, there is southeasterly wind in a layer from 300 to 400 m. The lidar images (Figs. 10 and 11) also indicate that 300–400 m is where the southern and northern MBL meet. There is no doubt that there has to be at least some influence of the southern MBL which is moving westward and impinging on the northwesterly flow moving around Point Conception. The middle layer that has easterly flow in the Santa Barbara Channel must slow and change direction as it encounters the northwesterly flow. It is clear from the sounding in Fig. 11 that an easterly wind layer is present from about 280 to 580 m. The isobaric legs were flown near 220 m, just below the middle layer, so the change of the wind in the 300-m thick layer just above the aircraft is not clearly reflected in those low-level legs. There is some indication of this in set E (Fig. 8) when the wind becomes easterly at the end of the leg. However, it is reasonable to infer that there is a region of enhanced confluence or convergence near the cloud edge. A complete description of the flow including quantifying the amount of convergence and confluence at several isobaric levels is challenging to explain completely because the measurements can only cover so much during the flight
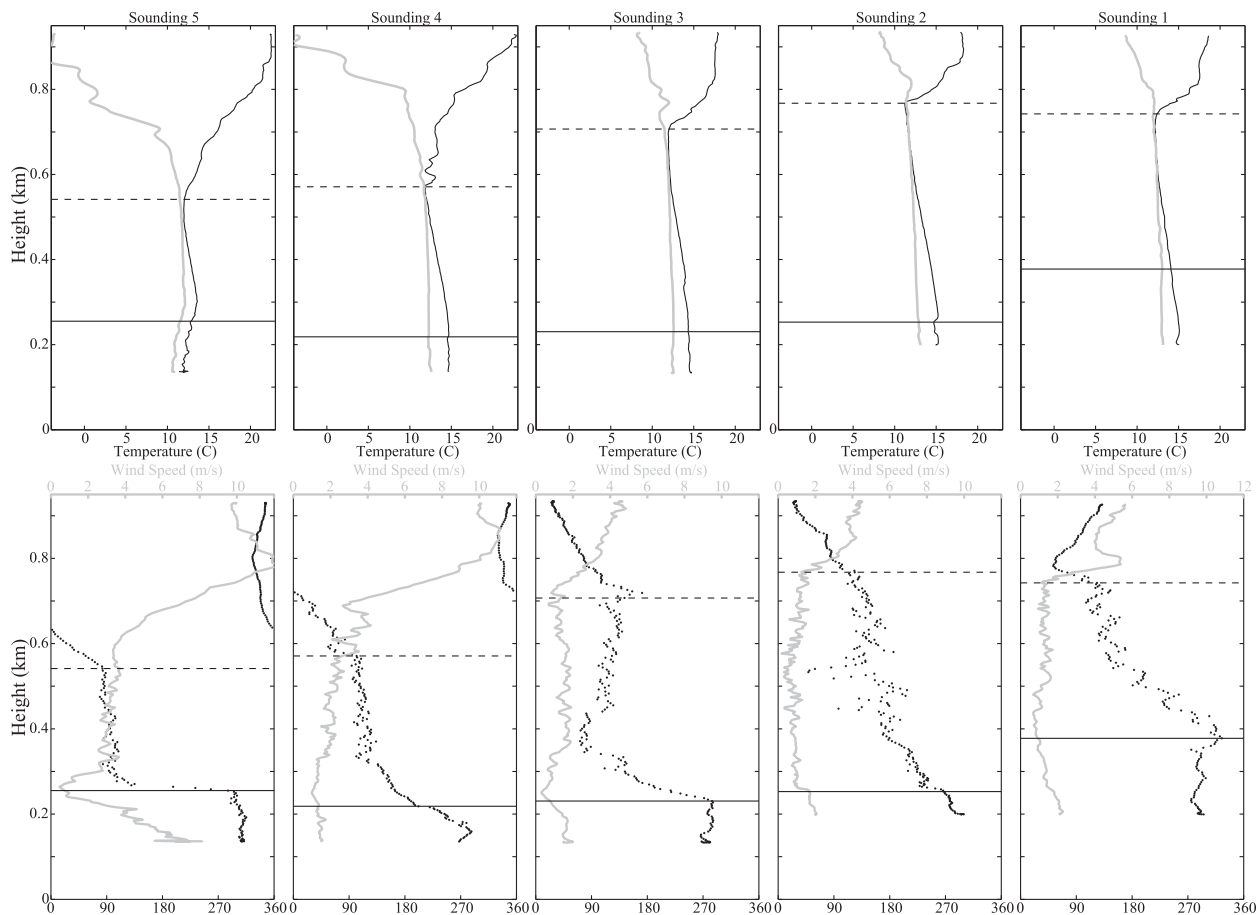
FIG. 14. Profiles of for each sounding indicated above for the (top) temperature (°C, black) and dewpoint temperature (°C, gray) and (bottom) wind speed (m s^{-1}, gray) and wind direction (degrees, black dots). Subjectively determined layers indicated by the horizontal lines.

and the numerical model results, which normally can be used to supplement the observations, have so much difficulty correctly representing such details of the flow.

Since model results of the MBL are questionable and few direct observations exist of the actual slope in the MBL height around Point Conception, it is not possible to generalize on how common or rare this type of situation is. Nevertheless, we do want to mention that the slope of the MBL height around Point Conception was much more gradual during other PreAMBLE flights. One of these cases was on 19 May 2012 when there was no Catalina eddy circulation (Rahn et al. 2013). On 19 May the MBL height dropped 200 m over 20 km. The lidar reflectivity for the 3 June case indicates a sudden drop of 300 m over just tens of meters. It cannot be generalized to all cases, but it is hypothesized that because there is this easterly zonal component for this 3 June 2012 case, an additional "sharpening" of the MBL occurs along a confluence/convergence zone between the southern and northern MBL.

Not only is there a sharp edge right next to the coastline, but this feature extends for at least 70 km southsouthwest of the topography. This is roughly on the scale of the cyclonic circulation occurring within the bight. The border between the northerly wind and the cyclonic circulation continues far to the southwest of Point Conception, thus the interaction of the layers is thought to contribute greatly to maintaining the sharp cloud so far away from the coastal topography. An impressive photograph taken during the flight on 3 June 2012 revealed a nearly vertical jump in cloud top 70 km away from the topography (Fig. 16). This is where the middle layer thins and encounters the northerly flow and so is not very deep and would be associated with being near 2123:30 UTC in the lidar image of Fig. 11.

4. Conclusions

Airborne measurements on 3 June 2012 reveal a complex interaction near Point Conception between
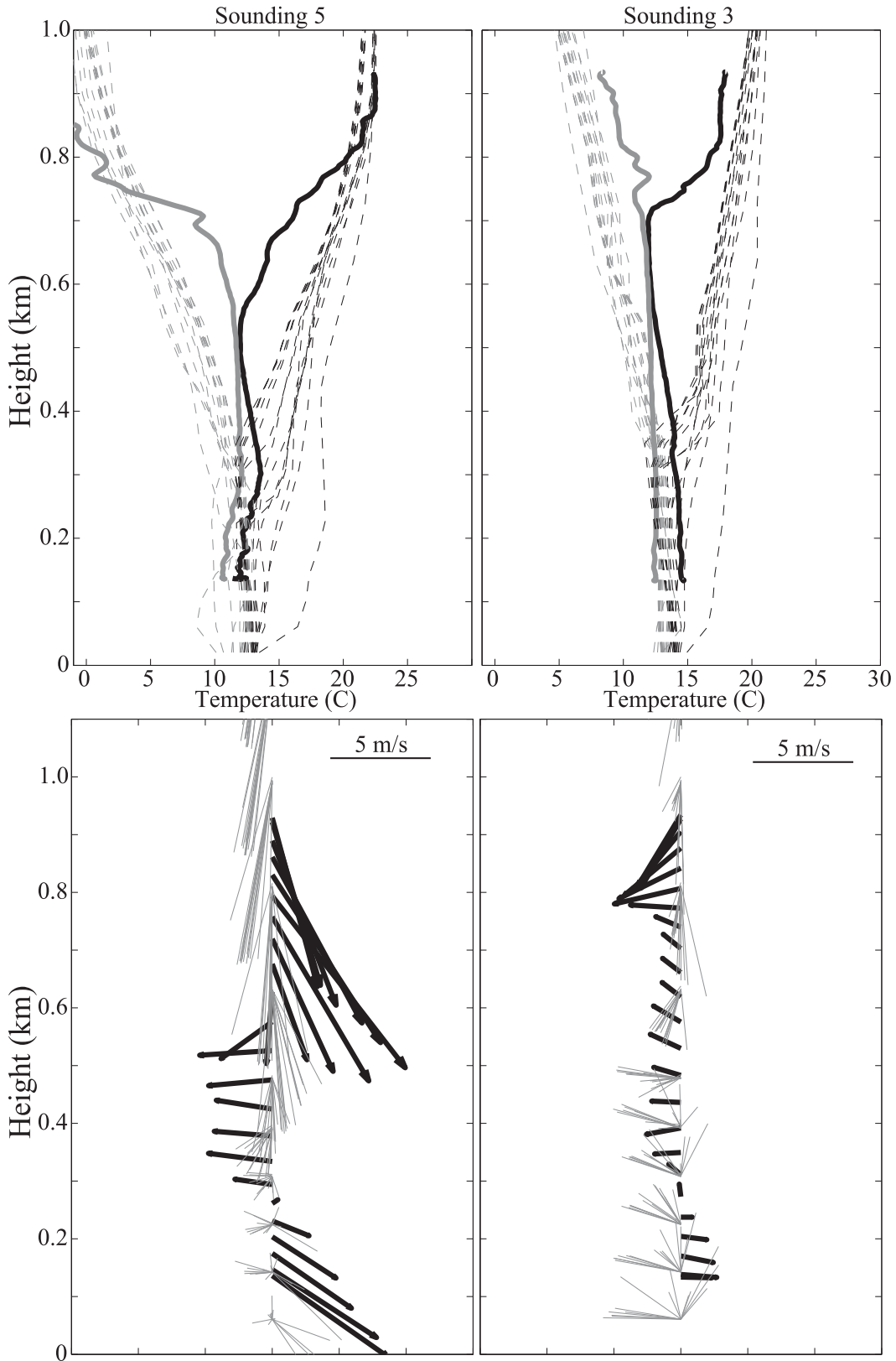
FIG. 15. (top) Comparison of observed temperature (°C, bold black) and dewpoint temperature (°C, bold gray) to 14 different WRF configurations (thin dashed). (bottom) Wind vectors of the observed (bold black) and modeled (thin gray) wind of the 14 different WRF configurations. Every tenth wind observation is shown, and only every other model grid point is used starting from the second level.

FIG. 16. Photo taken from the green circle in Fig. 11a.

two distinct MBLs that originate from north and south of Point Conception. It is hypothesized that this case differs from the classic depiction of a coastal jet whose forcing is interpreted by solely mechanical features within a two-layer shallow-water system (e.g., Dorman and Koračin 2008). The major difference is that the northerly flow in the MBL encounters an opposing wind and a slightly warmer MBL associated with a cyclonic circulation in the California Bight. Thus, even if there is the classic thinning of the MBL and increase of wind speed, the flow must be also modified to some extent by the conditions in the Santa Barbara channel that the term expansion fan should not be used in this case since it connotes an unperturbed mechanical response to only a change in the orientation of the coastline and no other external factors. Instead, the suite of observations suggests that just south of Point Conception there is a three-layer system. The three layers are identified using profiles of the temperature, dewpoint temperature, and wind. The lowest layer is the northern MBL that has north-westerly flow and is the coldest with a virtual potential temperature of 286.8 K increasing to 290.3 K. The middle layer is the southern MBL that has easterly flow and is cool with a constant virtual potential temperature of 290.3 K in the entire layer. The top layer is the warm and dry free troposphere that is separated from the middle layer by a marked subsidence inversion.

A sharp cloud edge extends south-southwest near the level where the northern MBL and the southern MBL meet and is associated with the interface between the cyclonic circulation and the northerly wind. Evidence for this comes from the in situ measurements combined with the lidar imagery that suggest opposing flow between 280 and 580 m, which is near the cloud level. At 2000–2200 UTC buoy measurements indicate that the cyclonic circulation farther south in the California Bight has strengthened so that the pressure gradient both to the north and to the south is pointing toward Vandenberg.

Study of the complex situation of the 3 June 2012 case here has been limited to just observations. Various numerical simulations with different grid spacing (down to 1 km) and parameterizations were conducted. The model solutions yielded mixed results since it is difficult to capture such complex interactions occurring on a relatively small scale. One other major issue is the timing, because the simulations tend to dissipate the easterly flow much sooner than reality. As a result, direct comparison with observations taken on 3 June 2012 show too many differences to confidently use the model as an additional source of data at this time. Correctly simulating the 3 June 2012 case is likely a hard test for most of the current numerical models.

REFERENCES

Burk, S. D., and W. T. Thompson, 1996: The summertime low-level jet and marine boundary layer structure along the California coast. *Mon. Wea. Rev.,* **124,** 668–686.

——, and ——, 2004: Mesoscale eddy formation and shock features associated with a coastally trapped disturbance. *Mon. Wea. Rev.,* **132,** 2204–2223.

——, T. Haack, and R. M. Samelson, 1999: Mesoscale simulation of supercritical, subcritical, and transcritical flow along coastal topography. *J. Atmos. Sci.,* **56,** 2780–2795.

Chou, M.-D., and M. J. Suarez, 2000: A solar radiation parameterization for atmospheric studies. Vol. 11, NASA Tech. Memo. 104606, NASA Goddard Space Flight Center, Greenbelt, MD, 40 pp.

Dorman, C. E., and C. D. Winant, 2000: The structure and variability of the marine atmosphere around the Santa Barbara Channel. *Mon. Wea. Rev.,* **128,** 261–282.

——, and D. Koračin, 2008: Response of the summer marine layer flow to an extreme California coastal bend. *Mon. Wea. Rev.,* **136,** 2894–2992.

——, D. P. Rogers, W. Nuss, and W. T. Thompson, 1999: Adjustment of the summer marine boundary layer around Point Sur, California. *Mon. Wea. Rev.,* **127,** 2143–2159.

——, T. Holt, D. P. Rogers, and K. Edwards, 2000: Large-scale structure of the June–July 1996 marine boundary layer along California and Oregon. *Mon. Wea. Rev.,* **128,** 1632–1652.

Dudhia, J., 1989: Numerical study of convection observed during the winter monsoon experiment using a mesoscale two-dimensional model. *J. Atmos. Sci.,* **46,** 3077–3107.

Edinger, J. G., and M. G. Wurtele, 1972: Interpretation of some phenomena observed in southern California stratus. *Mon. Wea. Rev.,* **100,** 389–398.

Edwards, K. A., A. M. Rogerson, C. D. Winant, and D. P. Rogers, 2001: Adjustment of the marine atmospheric boundary layer to a coastal cape. *J. Atmos. Sci.,* **58,** 1511–1528.

Haack, T., S. D. Burk, C. Dorman, and D. Rodgers, 2001: Supercritical flow interaction within the Cape Blanco–Cape Mendocino orographic complex. *Mon. Wea. Rev.,* **129,** 688–708.

Koračin, D., and C. E. Dorman, 2001: Marine atmospheric boundary divergence and clouds along California in June 1996. *Mon. Wea. Rev.,* **129,** 2040–2056.

——, ——, and E. P. Deaver, 2004: Coastal perturbations of marine-layer winds, wind stress, and wind stress curl along California and Baja California in June 1999. *J. Phys. Oceanogr.,* **34,** 1152–1172.

MacCready, P. B., Jr., 1964: Standardization of gustiness values from aircraft. *J. Appl. Meteor.,* **3,** 439–449.

Mass, C. F., and M. D. Albright, 1989: Origin of the Catalina eddy. *Mon. Wea. Rev.,* **117,** 2406–2436.

Parish, T. R., and D. Leon, 2013: Measurement of cloud perturbation pressures using an instrumented aircraft. *J. Atmos. Oceanic Technol.,* **30,** 215–229.

——, M. D. Burkhart, and A. R. Rodi, 2007: Determination of the horizontal pressure gradient force using Global Positioning System on board an instrumented aircraft. *J. Atmos. Oceanic Technol.,* **24,** 521–528.

——, D. A. Rahn, and D. Leon, 2013: Airborne observations of a Catalina eddy. *Mon. Wea. Rev.,* **141,** 3300–3313.

Pleim, J. E., 2006: A simple, efficient solution of flux–profile relationships in the atmospheric surface layer. *J. Appl. Meteor. Climatol.,* **45,** 341–347.

——, 2007: A combined local and nonlocal closure model for the atmospheric boundary layer. Part I: Model description and testing. *J. Appl. Meteor. Climatol.,* **46,** 1383–1395.

——, and A. Xiu, 2003: Development of a land-surface model. Part II: Data assimilation. *J. Appl. Meteor.,* **42,** 1811–1822.

Rahn, D. A., and T. R. Parish, 2007: Diagnosis of the forcing and structure of the coastal jet near Cape Mendocino using in situ observations and numerical simulations. *J. Appl. Meteor. Climatol.,* **46,** 1455–1468.

——, ——, and D. Leon, 2013: Coastal jet adjustment near Point Conception, California, with calm conditions in the bight. *Mon. Wea. Rev.,* **141,** 3827–3839.

Rodi, A. R., and T. R. Parish, 1988: Aircraft measurement of mesoscale pressure gradients and ageostrophic winds. *J. Atmos. Oceanic Technol.,* **5,** 91–101.

Rogers, D. P., and Coauthors, 1998: Highlights of Coastal Waves 1996. *Bull. Amer. Meteor. Soc.,* **79,** 1307–1326.

Rogerson, A. M., 1999: Transcritical flows in the coastal marine atmospheric boundary layer. *J. Atmos. Sci.,* **56,** 2761–2779.

Saha, S., and Coauthors, 2010: The NCEP Climate Forecast System Reanalysis. *Bull. Amer. Meteor. Soc.,* **91,** 1015–1057.

Samelson, R. M., 1992: Supercritical marine-layer flow along a smoothly varying coastline. *J. Atmos. Sci.,* **49,** 1571–1584.

Schroeder, I. D., B. A. Black, W. J. Sydeman, S. J. Bograd, E. L. Hazen, J. A. Santora, and B. K. Wells, 2013: The North Pacific high and wintertime preconditioning of California current productivity. *Geophys. Res. Lett.,* **40,** 541–546, doi:10.1002/grl.50100.

Skamarock, W. C., J. B. Klemp, J. Dudhia, D. O. Gill, D. M. Barker, W. Wang, and J. G. Powers, 2008: A description of the Advanced Research WRF version 3. NCAR Tech. Note NCAR/TN-475+STR, 113 pp.

Skyllingstad, E. D., P. Barbour, and C. E. Dorman, 2001: The dynamics of northwest summer winds over the Santa Barbara Channel. *Mon. Wea. Rev.,* **129,** 1042–1061.

Thompson, G., P. R. Field, R. M. Rasmussen, and W. D. Hall, 2008: Explicit forecasts of winter precipitation using an improved bulk microphysics scheme. Part II: Implementation of a new snow parameterization. *Mon. Wea. Rev.,* **136,** 5095–5115.

Thompson, W. T., S. D. Burk, and J. Rosenthal, 1997: Investigation of the Catalina eddy. *Mon. Wea. Rev.,* **125,** 1135–1146.

Tjernström, M., and B. Grisogono, 2000: Simulations of supercritical flow around points and capes in a coastal atmosphere. *J. Atmos. Sci.,* **57,** 108–135.

Wakimoto, R. M., 1987: The Catalina eddy and its effect on pollution over southern California. *Mon. Wea. Rev.,* **115,** 837–855.

Wang, Z., P. Wechsler, W. Kuestner, J. French, A. Rodi, B. Glover, M. Burkhart, and D. Lukens, 2009: Wyoming cloud lidar: Instrument description and applications. *Opt. Express,* **17,** 13 576–13 587.

——, and Coauthors, 2012: Single aircraft integration of remote sensing and in situ sampling for the study of cloud microphysics and dynamics. *Bull. Amer. Meteor. Soc.,* **93,** 653–668.

Winant, C. D., C. E. Dorman, C. A. Friehe, and R. C. Beardsley, 1988: The marine boundary layer off northern California: An example of supercritical channel flow. *J. Atmos. Sci.,* **45,** 3588–3605.

Xiu, A., and J. E. Pleim, 2001: Development of a land surface model. Part I: Application in a mesoscale meteorological model. *J. Appl. Meteor.,* **40,** 192–209.